Shock-Vortex Interactions at High Mach Numbers

Audrey Rault,[1] Guillaume Chiavassa,[1] and Rosa Donat[2]

We perform a computational study of the interaction of a planar shock wave with a cylindrical vortex. We use a particularly robust High Resolution Shock Capturing scheme, Marquina's scheme, to obtain high quality, high resolution numerical simulations of the interaction. In the case of a very-strong shock/vortex encounter, we observe a severe reorganization of the flow field in the downstream region, which seems to be due mainly to the strength of the shock. The numerical data is analyzed to study the driving mechanisms for the production of vorticity in the interaction.

KEY WORDS: Shock capturing schemes; composite vortex; shock deformation.

1. INTRODUCTION

The study of shock wave/vortex encounters has been a fertile field of investigation for several decades. The interaction of a concentrated vortex and a shock wave may occur in many situations of practical interest. In the operational environment of supersonic aircraft and missiles, the interaction may be a result of vortices created by the forward components of a supersonic vehicle convecting downstream and interacting with shock waves formed over aft surfaces or shock waves present in front of the air intake system of the vehicle, leading to performance deterioration [32]. In addition, the "shock-associated noise" generated in the interaction is an important factor in the design of advanced jet engines because of the effect on community noise and aircraft interior noise, among other things. Other fields where the study of shock vortex encounters is of importance include the case of helicopter blades operating at supercritical speeds [25] and fuel-air mixing enhancement in the combustor of a supersonic combustion ramjet [32].

Much of the early work on this problem was motivated by an interest in understanding the noise production mechanism and hence the research was directed towards the production and evolution of acoustic waves (see [13] and references therein). The early studies on shock-vortex interactions focused primarily on the

---

[1] LATP and ESM2, Marseille. E-mail: rault@cmi.univ-mrs.fr, guillaume.chiavassa@esm2.imt-mrs.fr
[2] Departamento de Matemàtica Aplicada, Universitat de València, València, Spain. E-mail: donat @uv.es

development of predictive linear theories that were compared with experimental results. Later on, research efforts concentrated on the use of numerical methods for analyzing the problem. Some of the first successful numerical techniques included finite-difference schemes or spectral methods to solve the Euler equations coupled with shock fitting techniques across the shock (see, e.g., references in [25, 14]). Indeed, the early time behavior of the flow field generated in a shock/vortex encounter can become quite complex, depending on the strength of both the shock wave and the vortex field. Shock fitting techniques have been used with success [15, 14], but it is generally agreed that they are difficult to apply in cases of strong interactions. The *shock-capturing* approach seems to have been first considered in [25], and schemes of the *shock-capturing* family have been commonly used in the last decade [13, 3, 17, 16]. The use of state of the art High Resolution Shock Capturing (HRSC) schemes has been reported in recent studies of various aspects of the shock/vortex interaction problem [1, 15, 19].

The case of *very strong* shock vortex encounters has only been considered fairly recently. In most of the aforementioned references the parameter range for the shock Mach number M_s is $[\approx 1, 2]$, $M_s = 2$ being considered a strong shock wave. However, current wind tunnel facilities are capable of attaining $M_s = 4$ [32], and there is a growing interest in the simulation of shock/vortex encounters at high Mach numbers [15, 14].

In this paper we advocate the use of a certain state-of-the art HRSC scheme, Marquina's scheme with the Piecewise Hyperbolic Method (a piecewise hyperbolic ENO-type reconstruction technique, see [24]) for the computation of the numerical flux functions. The M-PHM scheme (see [9] and Sec. 3 for details) is a formally third order accurate, both in space and in time, HRSC scheme which has been shown to be very robust; leading to well behaved, essentially oscillation free numerical solutions, in situations where pathological behavior is known to occur with other HRSC schemes (see [9]).

The basic numerical technique was originally developed in [9] and follows closely Shu and Osher's formulation in multidimensions [31] to obtain the numerical fluxes needed for a scheme in conservation form, i.e., with the shock capturing property. It is, therefore, very simple to implement on Cartesian grids (simpler than spectral techniques of the kind used in [7, 3]) and, when combined with a sufficiently fine numerical mesh, has all the ingredients necessary to carry out a high quality, high-resolution numerical simulation of the shock/vortex interaction problem.

It is well known, however, that high-order HRSC schemes tend to be quite expensive. This is particularly true for the scheme of our choice [9, 4]; therefore computations on very fine meshes tend to have a prohibitive cost unless a large computing facility is available.

The last two authors addressed this issue in [4], where they develop a multilevel technique designed to reduce the computing time of a HRSC numerical simulation on a fine-mesh. All the numerical simulations in this paper have been obtained with the multilevel work-reduction technique described in [4] applied to the M-PHM scheme; we have dubbed the resulting numerical technique the M&M-PHM scheme.

With the aid of the M&M-PHM scheme, we have been able to investigate –on a personal computer—the phenomenology of the shock-vortex interaction problem for a wide range of shock and vortex strengths. Our extensive numerical experimentation allows us to explore the different flow patterns that can develop after the interaction. We are able to reproduce all the flow features described in earlier studies and, for very strong interactions, we observe very particular flow patterns. A very strong ($M_s \geqslant 4$) shock wave produces a significant disruption of the vorticity pattern that can happen almost immediately after the interaction. It seems that a strong disorganization of the vortical structure has been observed in recent experimental studies [32]. We thus concentrate in the study of the flow field downstream of the shock wave for very strong interactions, and on the mechanisms of production of vorticity in these encounters.

The paper is organized as follows: In Sec. 2 we follow closely previous work of [13] to describe the physical setting and the phenomenology of the shock-vortex interaction problem we use as a test case in our numerical simulations. Section 3 gives a brief overview of the numerical technique employed in our simulations: the M&M-PHM scheme. Section 4 is dedicated to the analysis and interpretation of the data obtained in our parametric study. In Secs. 4.1 and 4.2, we show numerical simulations for a range of parameters covered in previous computational studies and perform a limited grid sensitivity study of the strong interaction case. The analysis performed serves to validate our numerical technique.

In Sec. 4.3 we turn to consider the very-strong interaction case, and show numerical simulations that display the abrupt reorganization of the initial vortex, upon crossing a strong shock wave. In Sec. 5 we focus our attention to the production of vorticity during the interaction. In Sec. 6 we compare the vorticity jump across the shock obtained from our simulations with a theoretical result given by Kevlahan in [22]. Conclusions and perspectives are drawn in Sec. 7.

2. THE INTERACTION OF A PLANAR SHOCK WITH A ROTATING VORTEX

2.1. Model Problem and Initial Conditions

To model the dynamics of the interaction, we follow [13] and assume that the flow is governed by the two-dimensional Euler equations

$$\partial_t \vec{\mathscr{U}} + \vec{f}(\vec{\mathscr{U}})_x + \vec{g}(\vec{\mathscr{U}})_y = \vec{0}. \tag{1}$$

where $\vec{\mathscr{U}}$ is the vector of conserved quantities ($\rho, \rho u, \rho v, e$) and $\vec{f}(\vec{\mathscr{U}})$ and $\vec{g}(\vec{\mathscr{U}})$ the classical physical flux functions. The system is closed by the equation of state for a polytropic gas:

$$P = (\gamma - 1)(e - \tfrac{1}{2}\rho(u^2 + v^2)), \tag{2}$$

with the ratio of specific heats $\gamma = 1.4$ for air.

A composite vortex, as described in [13, 16, 17], consists of an inner core of uniform vorticity with total circulation Γ^+ and an outer annular region of uniform
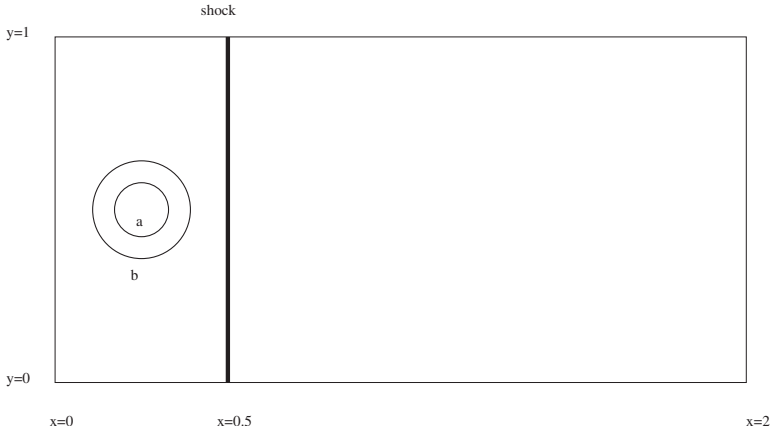
Fig. 1. Schematic representation of the initial condition for the numerical simulations.

and oppositely directed vorticity with total circulation $\Gamma^- = -\Gamma^+$. For the single vortex problem, the velocity is counter clockwise in both regions, with an angular velocity given by

$$
v_\theta = \begin{cases}
v_m \dfrac{r}{a} & \text{if } r \leqslant a \\[2ex]
v_m \dfrac{a}{a^2 - b^2}\left(r - \dfrac{b^2}{r}\right) & \text{if } a \leqslant r \leqslant b \\[2ex]
0 & \text{if } r > b
\end{cases}
$$

where v_m represents the maximal angular velocity, which occurs at $r = a$.

At $t = 0$ we consider a stationary shock totally isolated from the rotating vortex. The situation is depicted in Fig. 1, where we consider a rectangular computational domain, $\Omega = [0, 2] \times [0, 1]$. The shock is located at $x = 0.5$ and the center of the vortex is located at the point $(0.25, 0.5)$. The inner core radius $a = 0.075$ and the outer annular region has a maximum radius $b = 0.175$.

Outside of the vortex, the parameters of the flow are specified by $\rho_1 = 1$, $u_1 = \sqrt{\gamma}\, M_s$, $v_1 = 0$, $P_1 = 1$ at the left side of the shock (the supersonic region), and by ρ_2, u_2, v_2, P_2 at the right side (the subsonic region). The right quantities are determined from the left ones by writing the stationarity condition for the shock.

Inside the vortex, pressure, density and energy are determined by balancing the pressure gradients with the centripetal force, which amounts to solving the following system (see also [13, 16]):

$$
\frac{dP}{dr} = \rho\, \frac{v_\theta^2}{r}, \qquad P = \rho RT, \qquad \frac{P}{\rho^\gamma} = K
$$

where K is a constant. From the last two equations it is fairly straightforward to deduce that the pressure and density fields inside the vortex satisfy

$$P = P_1 \left(\frac{T}{T_1} \right)^{\frac{\gamma}{\gamma-1}} \qquad \rho = \rho_1 \left(\frac{T}{T_1} \right)^{\frac{1}{\gamma-1}}. \tag{3}$$

Using these equations we integrate the following ordinary differential equation to obtain the temperature:

$$\frac{dT}{dr} = \frac{\gamma-1}{R\gamma} \frac{v_\theta^2}{r}.$$

The expression of T, together with (3) allows us to compute the pressure and density distribution inside the vortex. The radial velocity is added to the free stream velocity to determine the velocity field inside the vortex, i.e., $(u, v) = (u_1, v_1) + v_\theta(-\sin\theta, \cos\theta)$. Finally, energy is computed in the whole domain via Eq. (2).

In all our simulations we have considered inflow boundary conditions at $x = 0$ and outflow for the other boundaries. In a setting like the one considered here the domain boundaries do not directly affect the vortex field because the range of influence of the composite vortex is finite [13, 16].

We take $M_v = v_m/c_1 = v_m/\sqrt{\gamma}$ as a measure of the strength of the vortex, since it is directly related to the maximum speed of rotation inside of the vortex, v_m.

2.2. Phenomenology

In the situation described in the previous section, the vortex is convected by the supersonic free-stream until it reaches the shock. The effect of the vortex on the shock profile depends strongly on the relative strengths of the shock and the vortex. If the vortex is weak relative to the shock, there is no significant distortion of the shock front, and the situation corresponds to that described in theoretical analysis that assume only small perturbations of the planar front [29].

A strong vortex however, distorts both a weak and a strong shock in such a way that the structure of the transmitted shock is much more complex. At the early stages of the interaction, the shock is distorted by the vortex in an S-structure (see [13, 1]) which can be clearly observed in the numerical simulation displayed in Fig. 2: the lower and upper portions of the shock are diffracted around the vortex, and the two diffracted shocks are connected by a refracted shock which passes through the core of the vortex. The shock structure at later stages depends on the strength of the shock relative to the vortex [1]. If the shock is weak relative to the vortex the interaction leads to a shock structure similar to that of a regular reflection, while increasing M_s and keeping the vortex unchanged leads to a Mach reflection structure instead. It must be mentioned that in [13, 1], $M_s = 1.05$ is considered weak, while $M_s = 1.5$ is considered strong and their computations cover only the range $M_s \in [1, 1.5]$ for the shock strength.

An important byproduct of the interaction is the production and evolution of acoustic waves. This feature has been investigated from a theoretical point of view
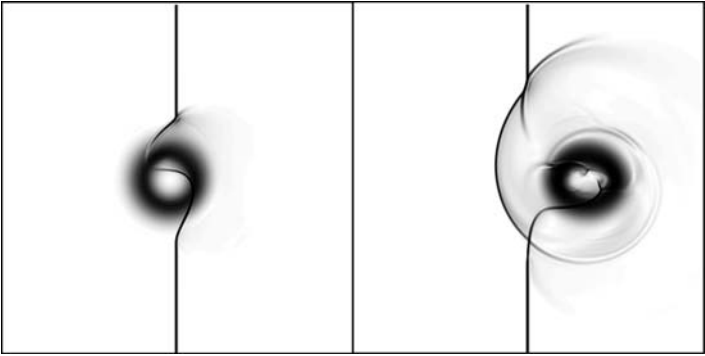
Fig. 2. Strong vortex-weak shock interaction for $(M_v, M_s) = (1.7, 1.1)$ at $t = 0.18$ and $t = 0.35$. Numerical Schlieren images obtained with the density.

[29] and in numerous computational studies [25, 13, 16, 17, 19, 20]. In these references, the authors are mainly concerned with the form of the acoustic wave for later times after the interaction. They find, both theoretically and numerically, that for weak vortices a cylindrical acoustic wave is generated for which the peak sound pressure in a circle of given radius varies from positive to negative twice (quadrupolar); this quadrupolar acoustic wave produced by the interaction expands later radially outward of the vortex (see Fig. 4).

Simulations of the interaction of a rapidly rotating vortex with a strong shock for Mach numbers larger than 3 are much more scarce in the literature. For this particular model, the relation P_c/P_1 (the pressure dip at the center core) is ≈ 0.1 for $M_v = 1.2$, which is consistent with experimental measures of wing tip vortices [32]. For larger values of M_v the density and pressure drops are more intense. $M_v \sim 1.8$ is the largest vortex strength we can use in our simulations, since for stronger values the model of vortex we use gives non-physical parameters (negative temperature, density and pressure). We restrict our simulations to $M_v \leqslant 1.7$.

In this paper, the use of a very robust scheme for systems of conservation laws, allows us to perform numerical simulations for a wide range of shock and vortex strengths. These simulations demonstrate that an increasingly complex wave pattern takes place for shock strengths larger than 3. In Figs. 9 and 10, for example, it can be clearly observed that the initial vortex may split immediately after the interaction, into a number of smaller vortical structures. We shall focus our investigations on this less studied feature of the shock-vortex interaction problem.

The equation that governs the evolution of vorticity $\vec{\omega}$ in a two-dimensional inviscid fluid can be derived by taking the *curl* of the momentum equation. In doing so, we arrive at

$$\frac{d\vec{\omega}}{dt} = -\vec{\omega}(\vec{\nabla} \cdot \vec{\mathscr{V}}) + \frac{\vec{\nabla}\rho \times \vec{\nabla}p}{\rho^2}, \tag{4}$$

where $\vec{\omega} = \nabla \times \vec{\mathscr{V}}$ and $\vec{\mathscr{V}} = (u, v)$ is the velocity of the fluid.

Initially, the flow is irrotational away from the vortex. In the polytropic vortex $\vec{\nabla} \cdot \vec{\mathcal{V}} = 0$ and the gradients of density and pressure are aligned, hence the two source terms on the r.h.s. of (4) vanish and the vortex is carried away by the free stream. The situation changes drastically when the vortex reaches the shock; the two terms in the r.h.s. of (4) enter the scene leading to production of vorticity. The first one is non zero due to the fact that vorticity and $\vec{\nabla} \cdot \vec{\mathcal{V}}$ are both non zero in the same regions (near the shock). During the interaction the gradients of density and pressure become non-aligned, hence the second term in the r.h.s. of Eq. (4) also becomes non zero. Together, these two terms act as a source leading to production of vorticity, which can be quite significant in some cases.

The study of the process of generation of vorticity by the interaction of a shock with discrete inhomogeneities in a fluid has received some attention in the literature [22, 28, 30]. Even though both terms on the r.h.s. of (4) act as a source of vorticity, their relative role in the overall generation of vorticity in the interaction seems to depend on the type of fluid homogeneity interacting with the shock. It is shown in [28] that the baroclinic term $\vec{\nabla}p \times \vec{\nabla}\rho / \rho^2$ is the most important one for density inhomogeneities such as bubbles in a uniform flow, while in turbulent motion the dominant term is the expansion term $\vec{\omega}\vec{\nabla} \cdot \vec{\mathcal{V}}$ [22].

Our extensive numerical experimentation reveals that the interaction of a sufficiently strong shock with a rotating vortex leads to the creation of new vortices after the interaction, with a considerable increase in the net vorticity of the resulting flow. The production of vorticity will be thoroughly investigated, through the analysis of numerical data, in Sec. 5. In particular we study the evolution of vorticity with respect to the strengths of the shock, M_s, and the vortex, M_v, with the aim of determining what are the specific conditions under which new vortices will appear after the interaction.

3. THE M&M-PHM SCHEME

3.1. Marquina's Scheme

The basic scheme used in our numerical simulations is Marquina's scheme, a shock capturing technique for systems of hyperbolic conservation laws that has proven to be very robust in a large variety of test problems, even when more classical schemes were known to produce anomalous numerical behavior. It is precisely this feature, the robustness of the scheme with respect to numerical pathologies, what makes us prefer Marquina's scheme to other shock-capturing techniques.

The reader is referred to [9] for a detailed description of the numerical scheme and its properties, and to [8, 10, 18, 23] for examples of application of the scheme in several scenarios. Here we shall briefly outline its main features.

Our implementation follows the semi-discrete formulation described by Shu and Osher in [31]

$$\frac{d\vec{\mathcal{U}}_{ij}}{dt} + \frac{\vec{F}_{i+1/2, j} - \vec{F}_{i-1/2, j}}{\delta x} + \frac{\vec{G}_{i, j+1/2} - \vec{G}_{i, j-1/2}}{\delta y} = \vec{0} \tag{5}$$

where $\vec{\mathscr{U}}_{ij}$ is the numerical approximation of the solution at the grid point $(x_i = i\,\delta x,\ y_j = j\,\delta y)$, and $\vec{F}(\vec{w}_1,...,\vec{w}_{k+m})$ and $\vec{G}(\vec{w}_1,...,\vec{w}_{k+m})$ are numerical flux functions, consistent with the physical flux functions in (1).

The computation of each numerical flux function at each cell interface in Shu–Osher ENO schemes is carried out by using the spectral decomposition of the Jacobian matrix of the system; for $F_{i+1/2,\,j}$, $\mathscr{A}(\vec{\mathscr{U}}) = \partial\vec{f}/\partial\vec{\mathscr{U}}$ is evaluated at a value U^* which is some kind of average between U_L, U_R, the values at each side of the interface (usually the Roe average). Instead, Marquina's scheme uses directly the spectral information contained in each one of the *two* Jacobian matrices $\mathscr{A}(\vec{\mathscr{U}}_L)$, $\mathscr{A}(\vec{\mathscr{U}}_R)$ to produce the final numerical flux function at the interface.

The basic first order scheme is converted into a state of the art, HRSC technique by using a high order ENO-type reconstruction technique in the computation of the characteristic variables and fluxes at each cell interface, together with the third order TVD Runge–Kutta time discretization procedure specified in [31]. As in [9, 4], we have chosen the Piecewise Hyperbolic Method (PHM) described in [24] for the reconstruction step. The PHM is a piecewise hyperbolic ENO-type reconstruction technique that avoids using data across large gradients in the reconstruction process. The results in [9] seem to indicate that the PHM reconstruction is more robust than its polynomial counterpart, the ENO-3 technique described in [31], at similar cost.

The final scheme, the M-PHM scheme, turns out to be a particularly robust third order HRSC numerical scheme. In [18, 23] the robustness of the scheme in critical situations is linked to the use of the characteristic information at each cell interface, without any mixing in the presence of large gradients. The numerical computations in [18] clearly demonstrate that mixing information from both sides of a cell interface, such as in the averaging process involved in Roe's solver or in a numerical flux computation based on an averaged value between U_L and U_R, can lead to oscillatory behavior in certain simulations involving density inhomogeneities in compressible flows.

The computational cost of the M-PHM scheme increases (an additional 20% over Shu and Osher ENO-3 scheme based on an averaged Jacobian) because the evaluation of the numerical flux function in Marquina's third order scheme demands two full spectral decompositions, instead of simply one as in Roe's scheme or none as in other simpler alternatives like the HLLE [12] scheme.

Taking into account that the analysis of the vortex breakdown phenomena needs a large number of high quality/high resolution numerical simulations, it becomes imperative to carry out these computations in an efficient manner. Since memory requirements are not a major concern, we use a multilevel technique developed in [4] that is designed to obtain a numerical solution of the same quality, i.e., same resolution, as the one obtained with a HRSC scheme, but at a much lower cost.

3.2. The Multilevel Technique

In [4], the last two authors describe a multilevel work reduction technique for HRSC applied to hyperbolic conservation laws. The key observation is a well

known fact to users of HRSC schemes: highly sophisticated numerical flux functions are only needed in the neighborhood of a discontinuity or in the regions where singularities will develop. According to this observation, a reduction in the cost is possible if the highly sophisticated flux function, needed to obtain a high resolution simulation, is used only where it is absolutely necessary, i.e., at discontinuities and regions undergoing strong compression.

Multiresolution decompositions provide an appropriate tool to determine the regions of smoothness of a given set of data, that represent the values of a function. They can be used to analyze the local smoothness of $\vec{\mathcal{U}}_{ij}^n$ in order to locate singularities and compression regions (leading to shock formation). The hyperbolic nature of the equations together with the CFL condition limit the propagation of singularities, therefore the use of multiscale decompositions makes it possible to establish a technique that marks those locations where a sophisticated flux computation is absolutely needed.

The multilevel work reduction technique for a given HRSC scheme is carefully described in [4]. Given a computational mesh, which we consider to be sufficiently fine to resolve the desired features in the solution to our satisfaction, the multilevel technique works on a sequence of computational meshes, obtained by successive dyadic coarsening of the original, to produce a numerical solution on the original grid of the same quality as that produced by the direct use of the HRSC scheme on the finest grid, but at a much lower cost. For each time step, the algorithm follows these basic steps:

(1) Interpolatory wavelet transform of ρ^n (L levels of resolution). The rate of decay of the *wavelet* coefficients can be easily related to the local regularity of the underlying function, i.e., ρ_{ij}^n, whose smoothness we consider representative of the smoothness of $\vec{\mathcal{U}}_{ij}^n$.

(2) Smoothness analysis. A thresholding procedure is applied to the wavelet coefficients to detect (and mark) the location of the singularities of $\vec{\mathcal{U}}_{ij}^n$ and to control their propagation and the possible formation of new ones during the time step δt_n.

(3) Region dependent computation of numerical divergence $\vec{D}(\vec{\mathcal{U}})$. We start by applying the HRSC scheme on the coarsest grid (after L steps of dyadic coarsening). We then work by dyadic refinement and let the smoothness analysis decide how to carry out the computation of $\vec{D}(\vec{\mathcal{U}})$. The costly HRSC scheme is used only at regions identified as *non-smooth* in step 2.

(4) Time step evolution with Runge–Kutta scheme.

The effective reduction in the work load is, of course, problem dependent. As shown in [4], for the ENO-3 and M-PHM schemes, the multilevel technique is cost-effective when the percentage of numerical divergences computed with the HRSC scheme does not exceed 60%. In these circumstances, it leads to a reduction (that depends on the percentage) of the cpu time of the numerical simulation with respect to the one obtained by applying the HRSC scheme on the full grid. For the test cases reported in this paper the percentage of numerical divergence computations

with the M-PHM scheme never exceeded 30%, hence it corresponds to the type of situation for which the multilevel work reduction technique is specially adequate (see [4]). An effective CPU time reduction by an average factor of 3 in comparison with the direct simulation is obtained (hours of computer time on a PC-500 Mhz, instead of days).

4. NUMERICAL RESULTS

With the help of the M&M-PHM scheme, we have carried out a parametric study of the shock-vortex interaction problem described in Sec. 2.1. Our numerical tests cover the range of parameters $M_v = [0.1, 1.7]$, $M_s = [1.1, 10]$.

The numerical simulations have been obtained with an underlying Cartesian grid of 1024×512 cells and a number of resolution levels $L = 5$, i.e., the coarsest mesh considered is 32×16. The time step is variable and is computed, via the CFL condition for the finest grid, as described in, e.g., [33].

The thresholding parameter that determines the region dependent computation of $\vec{D}(\vec{\mathcal{U}})$ in the M&M-PHM scheme is set to $10^{-4} \max_{ijk}(|d_{ijk}^n|)$ where d_{ijk}^n are the wavelet coefficients of the density at time t_n: ρ^n.

At each time step we have access to all the primitive variables from which we compute easily vorticity, circulation and all the variables needed in our numerical studies. For visualization purposes we have used both contour plots and Schlieren-type images. Schlieren-type techniques are often used for the visualization of weak flow features, like pressure waves or density variations. Darker pixel values on the plot correspond to larger pressure (or density) fluctuations.

4.1. Shock-Vortex Interactions: Low to Moderate Strength

4.1.1. Shock Distortion and Vortex Deformation

From the early works on shock-vortex interaction, it is known that an initially planar shock wave undergoes a certain deformation as it interacts with a compressible vortex. Weak interactions involve only small perturbations of the shock profile, that are assumed to be of sinusoidal type in successful linear theories of sound production [29]. Linear theories, however, are no longer applicable to moderate to strong interactions for which the shock goes through successive phases of symmetric and nonsymmetric deformation leading to the formation of a complex shock structure which includes secondary shocks, and a gradual return to the planar configuration as the vortex is left behind.

For a fixed shock strength M_s, the deformation increases with the vortex strength (see, e.g., [13, 1]). After the work of Chatterjee [1], it is known that in order to form a Mach structure, the shock wave must be strong *relative* to the vortex. Decreasing M_s while keeping the vortex unchanged results in a transition to a transmitted shock structure completely devoid of Mach stem from an earlier well-defined Mach structure.

In Fig. 2 we display two snapshots of the interaction of a strong vortex $M_v = 1.7$ with a weak shock $M_s = 1.1$. The strength of the vortex causes a pronounced S-shape deformation, clearly observed on the left display, as described in

the aforementioned references. According to [1], the maximum deformation is seen to occur shortly after the vortex center crosses the shock wave, and the snapshot corresponds to a slightly previous instant in time. The right display in Fig. 2 shows a snapshot of a later time, when the transmitted shock is beyond the vortex field. The shock wave is weak *relative* to the vortex, hence the interaction pattern should be that of a regular reflection, in which the secondary shock structures join up with the primary shock at a single point. This is precisely the structure of the transmitted shock in the right display of Fig. 2.

In Fig. 3 we display a situation classified as *strong vortex-strong shock* interaction in [13]. The left display shows a snapshot at a time where the Mach structure in the transmitted shock is clearly appreciated. It is known [11] that the shock compresses an initially circular vortex into an elliptical shape, the elongation depending on the shock strength. The ellipsoidal shape of of the vortex after the passage of the shock wave is clearly observed on the left display in Fig. 3 (recently, Grasso and Pirozzoli [19] have shown that the deformation of the vortex increases with M_s at a slower rate than predicted in [11]). The right display of this same figure corresponds to an instant in time that is posterior to all the plots in [13, 1], and to a stronger interaction than those described in [19]. It shows the late time evolution of the flow field. In this case it is observed that the compression effects due to the shock passage on the vortex has given rise to two vortical structures well differentiated. We shall come back to this vortex splitting phenomenon later on.

4.1.2. Formation and Evolution of Acoustic Waves

The interaction between a columnar vortex and a planar shock wave is considered as a crude but deterministic model of the generation of shock noise by turbulence passing through the shock wave pattern of a supersonic jet. Early experiments [11] show that a cylindrical sound wave appears downstream of the shock, partly cut off by the shock. This acoustic wave is centered on the moving vortex core and both grows and convects.

The formation and evolution of acoustic ''noise'' in shock vortex encounters has been the subject of several theoretical [29] and computational studies [13, 20, 19]. As the vortex goes through the shock, a *precursor* wave is generated. Initially, this near-field first sound shows a dipolar directivity [20, 19], that changes into a quadrupolar behavior once the vortex has traversed the shock [13]. As the vortex
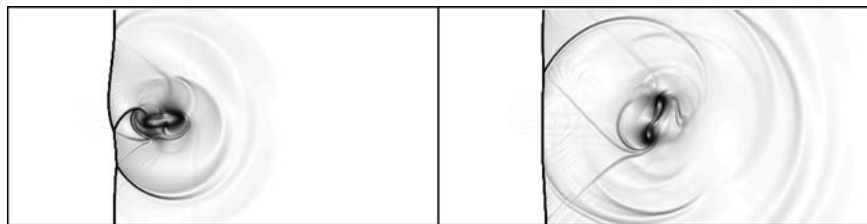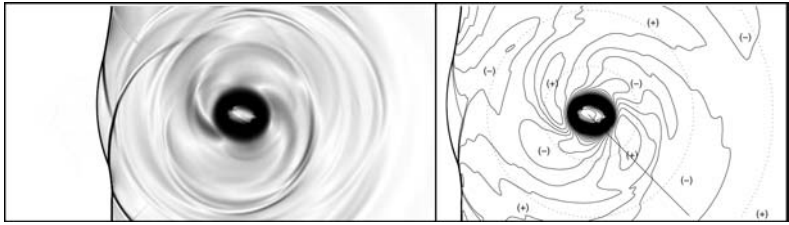

Fig. 3.   Shock-vortex interaction: $(M_v, M_s) = (0.9, 1.5)$, at two different times, left $t = 0.41$, right $t = 0.69$. Numerical Schlieren images obtained with the density.

Fig. 4. Strong vortex-weak shock interaction: Evolution of acoustic waves. $(M_v, M_s) = (1.7, 1.1)$ at time $t = 0.75$. Left: numerical Schlieren images obtained with the pressure. Right: contour plot of the overpressure. Compression zones are marked with $(+)$ and expansion regions with $(-)$. The dotted lines represent the location of the precursor, the second and the third acoustic waves. The straight line corresponds to angle $\Theta = -45°$.

moves downstream, the precursor expands radially and it is followed by a second sound of the same quadrupolar nature but not in phase with the precursor. At later stages a third sound is formed, in phase with the precursor. It is worth noticing that the occurrence of the third sound was hypothesized by Inoue and Hattori [20], but it was only observed in their parametric study for numerical simulations involving a vortex pair. Grasso and Pirozzoli [19] run their numerical simulations long enough to observe the occurrence of this third sound.

In our numerical simulations we have observed that the time at which the third sound is observed decreases when increasing M_v. The left display in Fig. 4 shows a Schlieren pressure plot of the flow of Fig. 2 but at a much later time, $t = 0.75$. The right display shows a contour plot of the same flow in which we have marked with a $(+)$ the compression zones $\Delta p > 0$ and with a $(-)$ the expansion regions $\Delta p < 0$, as in [20, 19]. In this plot we clearly observe the occurrence of three alternate
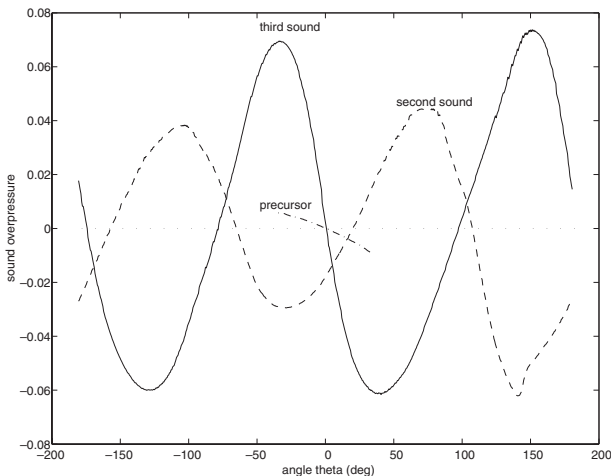

Fig. 5. Overpressure along the three acoustic waves.

compression and expansion regions . On Fig. 5 we plot the circumferential distribution of the pressure field $\Delta P = \frac{P-P_2}{P_2}$ for $(M_v, M_s) = (1.7, 1.1)$ at the three radii marked in Fig. 5 ($r = 0.85$ for the precursor, $r = 0.48$ for the second sound and $r = 0.22$ for the third sound, where r is the distance to the vortex core). The precursor is well in the far field, but we observe that, as expected, the circumferential variation of the second sound is opposite in sign with respect to the precursor and to the third sound.

In his theoretical study of sound production [29], Ribner argues that the precursor has a different nature from the second sound produced by the interaction. As a result, the acoustic pressure peak

$$\Delta P_m = \max_r \left| \frac{P-P_2}{P_2} \right|, \tag{6}$$

of the precursor decays with the radial distance r from the center of the vortex as r^{-1}, while for the second wave the decay is proportional to $r^{-1/2}$. In Fig. 6 we report the peak values ΔP_m, measured at $\Theta = -45°$, for the sound waves that we observe in the test case of Fig. 4. We observe that the peak sound pressure of the precursor follows the theoretical decay predicted by Ribner in [29], while for the other sound waves generated by the interaction, the peak sound pressure decays like $r^{-1/2}$.

Notice also that the acoustic pressure peaks are larger for the stronger vortex, a fact which has been remarked in [20, 19] and that is also observed in our simulations.
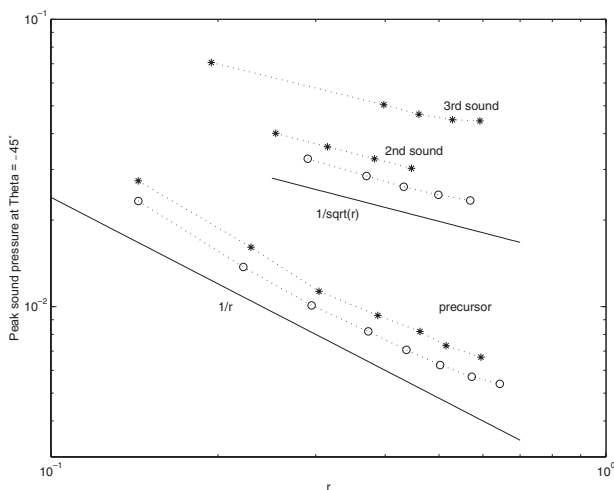
Fig. 6. Decay of ΔP_m versus r for the precursor and the remaining sound waves. ($\cdots \bigcirc \cdots$) correspond to the case $(M_v, M_s) = (1.1, 1.1)$ and ($\cdots * \cdots$) to a stronger vortex $(M_v, M_s) = (1.7, 1.1)$. Straight lines represent the theoretical decay.

4.2. Grid Sensitivity and Related Issues

The numerical simulations shown in the two previous subsections show a perfect qualitative and quantitative agreement with previous computational and theoretical studies that cover a much more limited parameter range.

In this section, we consider the case of very strong interactions and discuss the results from a purely numerical point of view, focussing on the influence of the multiresolution process and on the grid dependence of the numerical solution on the mesh parameters.

We run a direct simulation with the M-PHM scheme on the finest grid of a very strong interaction $(M_v, M_s) = (1.7, 4)$, and compare the numerical solution with that obtained with the M&M-PHM scheme. We found a relative difference between the density field in both simulations $\|\rho - \tilde{\rho}\|_1 / \|\tilde{\rho}\|_1 = 2 \cdot 10^{-3}$ (ρ is obtained with M&M-PHM and $\tilde{\rho}$ with M-PHM) after 2400 time steps, which corresponds to $t = 0.25$, when the interaction is completed and the vortex structure is well beyond the shock wave. This is absolutely consistent with the results in [4]: the effect of the multilevel work reduction technique is controlled by the smoothness parameter ϵ.

To examine the dependence of our numerical simulations on the mesh parameters we choose the test case $(M_v, M_s) = (1.2, 4)$ (the maximum pressure variation in the vortex $p_{center}/p_1 \approx 0.1$, which can be found in experimental measures of wing-tip vortices generated in wind tunnels [32]). We observe that the fine features of the flow field (in particular a second slip line downstream of the vortex) are only adequately resolved on the finer grid (see Figs. 7 and 8). All the other features of
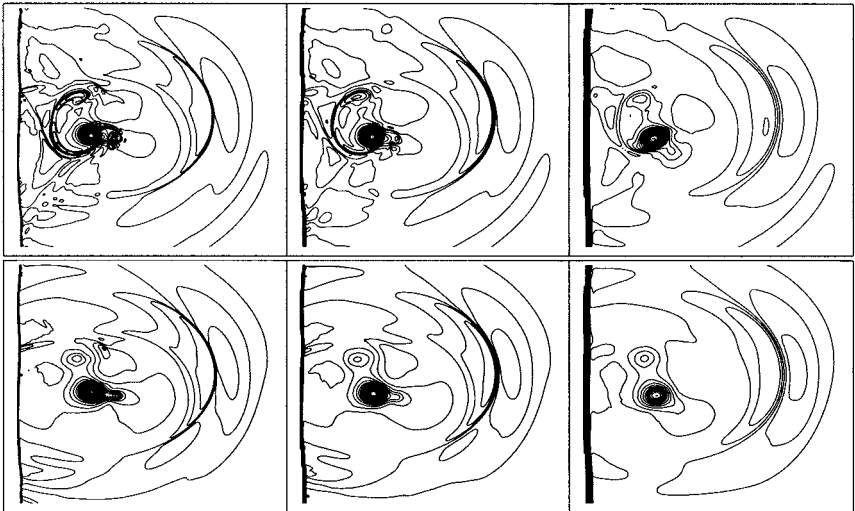

Fig. 7. $(M_v, M_s) = (1.2, 4)$ shock-vortex interaction at time $t = 0.25$, for multilevel M&M-PHM scheme. Left, 1024×512, $L = 5$; middle, 512×256, $L = 4$; right, 256×128, $L = 3$. Top: contour lines of density field. Bottom: contour lines of pressure field.
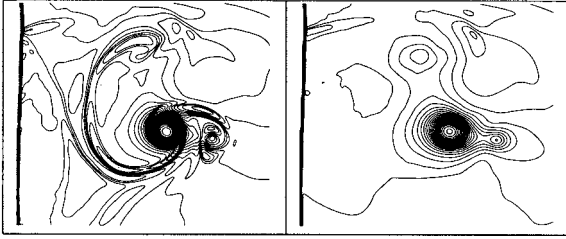
Fig. 8. Enlarged view of density (left) and pressure (right) fields in Fig. 7 (1024×512 resolution) around the vortex structure.

the flow, including the strong acoustic wave propagating ahead of the vortex are correctly represented in all three grids.

It is worth mentioning that the high resolution of the numerical simulation allows for a numerical determination of the speed at which the peak pressure moves in its radial expansion, once the quadrupolar structure is clearly recognized. Considering that after the interaction the vortex is advected by the flow with velocity $(u_2, v_2 = 0)$, the total velocity of the acoustic wave on the x-axis for $y = 0.5$ is then $u_2 + c_2$ where c_2 is the downstream sound speed. We found the numerically computed value for the speed to be within 1% of the predicted value (relative error).

4.2.1. Variation of Total Circulation

The last validation test concerns the total variation of the circulation Γ. Since we are working with a polytropic gas law, Kelvin's theorem applies, hence

$$\frac{d\Gamma}{dt} = 0.$$

Before the interaction the vortex satisfies by construction $\Gamma = 0$, then the total circulation has to remain zero during all the simulation. We defined the global circulation at time t as

$$\Gamma(t) = \int_\Omega \omega_z(x, y, t)\, dx\, dy = \int_\Omega \omega_z^+ + \int_\Omega \omega_z^-$$

where Ω is the computational domain and ω_z^+ and ω_z^- the positive and negative contributions of the vorticity. Consistency with physical principles dictates that $\Gamma^+(t) + \Gamma^-(t) = 0$ for all t. In our numerical simulations we check numerically this physical principle and obtain

$$\max_t \left| \frac{\Gamma^+(t) + \Gamma^-(t)}{\Gamma^+(t)} \right| < 0.01$$

(see Figs. 15 and 16 for various plots of $\Gamma^+(t)$).

4.3. Very Strong Shock/Vortex Encounters: The Effect of a Strong Shock on an Isolated Vortex

We shall consider now the effect of the shock on the dynamics of the vortex. Experimental [11] and computational [13, 19] studies show that the shock compresses an initially circular vortex into an elliptical shape whose axis depend on the shock strength. As observed in [13, 1, 20, 19], for $1 \lessgtr M_s$ the shock passage has little influence on the shape of the vortex, which keeps roughly its original shape (Figs. 2 and 4). The compression effects of strong shock waves on the dynamics of the vortex described in [19] can be clearly appreciated in Fig. 3; the elongation of the vortex gives rise, at later times, to two separate vortical structures.

Numerical experimentation with stronger shocks shows that the flow field may be quite different for larger Mach numbers. The vorticity field, in particular, seems to be strongly dependent on the shock strength.

In Fig. 9 we display three different patterns of the vorticity field after the interaction. The leftmost plot corresponds to $M_s = 1.5$ and a vortex of moderate strength ($M_v = 0.5$); we observe that the inner core of the vortex, composed of positive vorticity, is stretched and the outer negative ring begins to detach itself from the inner core. This stretching is more pronounced for larger values of M_s and/or M_v. For $M_s \sim 2$ (center plot in Fig. 9) and a slightly stronger vortex, the inner core and the outer annular region are stretched even more and two different structures seem to emerge after the interaction. For the range of parameters $1.5 \lessgtr M_s \lessgtr 2.5$, the shock wave unstabilizes the internal structure of the vortex. The late time evolution of the flow displays several separate structures (as an example, see right display in Fig. 3), but we can still recognize one connected vortical structure immediately after the interaction, as in Fig. 3, left display.

This situation should be compared with the extreme case shown in the rightmost display in Fig. 9, where the vorticity field presents a completely different pattern. The initial shape of the vortex can no longer be identified to any particular structure. The vorticity field seems to be completely reorganized immediately after
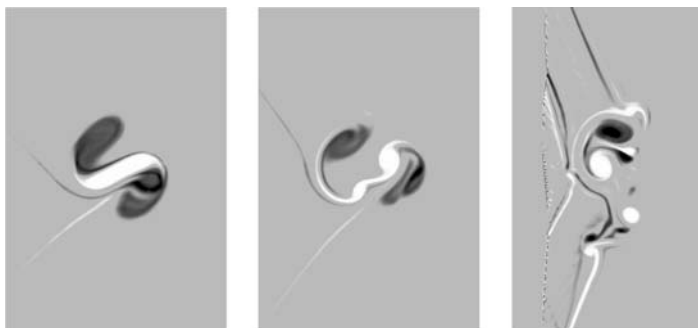
Fig. 9. Visualization of the vorticity field after the interaction. White color represents positive vorticity and black color negative vorticity. From left to right: $(M_v, M_s) = (0.5, 1.5)$ at $t = 0.7$, $(M_v, M_s) = (0.7, 2)$ at $t = 0.7$, and $(M_v, M_s) = (1.7, 7)$ at $t = 0.2$.
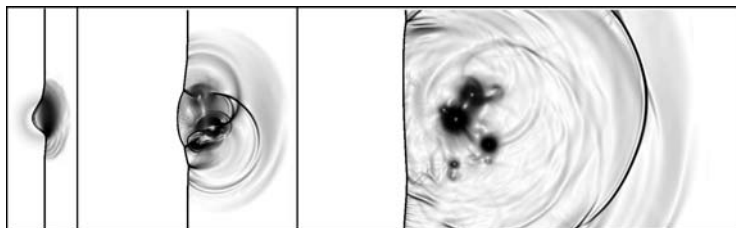
Fig. 10. Strong shock-vortex interaction: $(M_v, M_s) = (1.7, 7)$, at three different stages. Left, $t = 0.05$; middle, $t = 0.1$; right, $t = 0.25$. Numerical Schlieren images obtained with the pressure.

the shock passage into different independent vortical structures. In [32], a similar disruptive behavior is observed in experimental data concerning the interaction of streamwise tip vortices with oblique shock waves.

A Schlieren pressure image of the same simulation is displayed in Fig. 10, where we show the evolution of the flow at three different times. In the early-time plots we observe a strong deformation of the shock profile followed by an almost immediate splitting of the initial vortex into separate vortical structures. In addition a pressure peak, corresponding to a strong acoustic wave, propagates downstream at the sound speed, ahead of all the vortical structures (see Fig. 10, rightmost display). The pressure field downstream of the shock wave reveals the extremely complex structure of the flow field after a very strong interaction.

From the observational point of view, based on our extensive numerical experimentation, it seems that the flow pattern is more or less independent of the strength of the vortex, M_v. Slight differences can be observed on the shock deformation and/or the number of vortices that may emerge after the interaction. In Fig. 11 we show contour plots of the simulation corresponding to $M_s = 4$, $M_v = 1.7$. The structure of the flow field after the interaction should be compared with that in Figs. 7 and 8 which show the case for $M_v = 1.2$. In the case of Fig. 7, two vortical structures emerge after the interaction, while for the stronger vortex in Fig. 11 at least three can be observed.

The data obtained in our numerical simulations indicates that a strong "reorganization" of the vortex field takes place immediately after the interaction
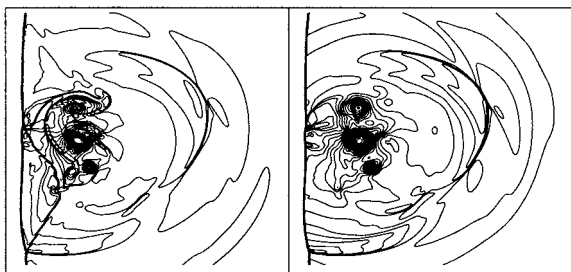

Fig. 11. Very strong shock-vortex interaction: $(M_v, M_s) = (1.7, 4)$, at $t = 0.25$. Contour plots of density (left) and pressure (right).

for sufficiently large vortex strengths. When this happens, it seems as if the shock would *break* the original vortex and, after the passage is complete, more than one vortical structure can be clearly recognized. We shall refer to this phenomenon as *(compressible) vortex breakdown*.

In the next sections, we turn to analyze in some detail the mechanisms for the production and evolution of vorticity with respect to the parameters M_v and M_s, as well as their relation to the vorticity pattern after the interaction.

5. VORTICITY PRODUCTION AND VORTEX BREAKDOWN

The interaction of a shock with a vortex comes associated to an increase in vorticity due to the action of the source terms in Eq. (4). We investigate the mechanisms leading to production of vorticity in the interaction by considering the time evolution of the enstrophy, defined as

$$E_s(t) = \tfrac{1}{2} \int_\Omega \omega_z^2(x, y, t) \, dx \, dy, \tag{7}$$

Using Eq. (4), it is easy to arrive at the following relation

$$\frac{\partial}{\partial t} \int_\Omega \omega^2 \, dS = \oint_{\partial \Omega} \omega^2 \vec{\mathcal{V}} \cdot \vec{n} \, dl - \int_\Omega \omega^2 \vec{\nabla} \cdot \vec{\mathcal{V}} \, dS + 2 \int_\Omega \vec{\omega} \cdot \frac{\vec{\nabla}\rho \times \vec{\nabla}p}{\rho^2} \tag{8}$$

where $\omega^2 = \omega_z^2$, Ω is the computational domain and the remaining variables are as in Sec. 2.1.

The computed enstrophy depends on the numerical viscosity of the scheme. In Fig. 12 we show the time evolution of the enstrophy for the test case $M_s = 4$, $M_v = 1.2$ in three different meshes. It is observed that not only the enstrophy peak, but also the value of $E_s(t)$ diminishes with numerical viscosity (larger mesh sizes), however, the shape of $E_s(t)$ remains the same. In order to assess the relative importance of the baroclinic and dilatational effects mentioned in Sec. 2.2, we compute
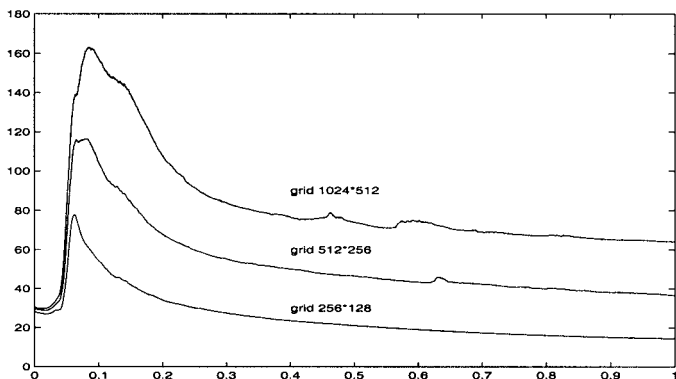

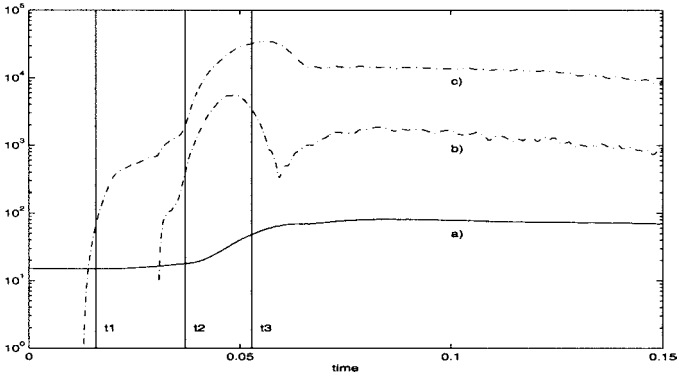**Fig. 12.** $(M_v, M_s) = (1.2, 4)$. Time evolution of Enstrophy $E_s(t)$ on three different meshes.

Fig. 13. $(M_v, M_s) = (1.2, 4)$. Time evolution of: (a) $E_s(t)$; (b) $2 \int_\Omega \omega \frac{\vec{\nabla}\rho \times \vec{\nabla}p}{\rho^2}$; (c) $-\int_\Omega \omega^2 \vec{\nabla} \cdot \vec{\mathcal{V}}$; see text for description of t_1, t_2, t_3.

$E_s(t)$ (using a simple quadrature rule), together with the contribution to the increase in enstrophy due to baroclinic effects (the last term in Eq. (8)) and dilatational effects (the second to last term in Eq. (8)) and show the results in Figs. 13 and 14.

Before the interaction, the vortex is advected by the flow. All terms in the r.h.s. of Eq. (8) are zero, therefore the enstrophy remains constant, as observed in Figs. 13 and 14, until the vortex flow field starts feeling the effects of the shock wave. If the vortex was simply passively advected by the flow, the times at which its outer and inner boundaries and its center would reach $x = 0.5$, the shock location, can be easily computed. For the parameters chosen in Fig. 13, ($M_v = 1.2$, $M_s = 4$), the time the outer region reaches the shock is $t_1 = 0.0158$ s, while the times the boundary of the undisturbed vortex core and its center would reach $x = 0.5$ would be respectively $t_2 = 0.037$ and $t_3 = 0.0528$. These three times have been marked also on the plot as vertical lines.
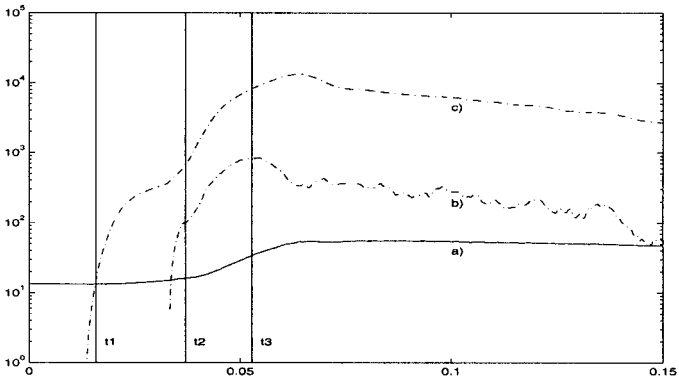

Fig. 14. $(M_v, M_s) = (0.8, 4)$. Time evolution of: (a) $E_s(t)$; (b) $2 \int_\Omega \omega \frac{\vec{\nabla}\rho \times \vec{\nabla}p}{\rho^2}$; (c) $-\int_\Omega \omega^2 \vec{\nabla} \cdot \vec{\mathcal{V}}$; see text for description of t_1, t_2, t_3.

As expected, the plotted terms begin to be non-zero only when the boundary of the outer annular region feels the influence of the shock ($\approx t_1$). A significant increase in enstrophy is only felt after $t \geqslant t_2$. After $t = t_3$ the shock is beyond the vortex core and the enstrophy is essentially constant again (it shows a slight decline, most likely due to numerical viscosity).

The plots in Figs. 13 and 14, where we repeat the computation for $M_v = 0.8$, $M_s = 4$, clearly show that the driving mechanism for the production of vorticity in the interaction (as it occurs also in turbulent motion [22]) is due to the expansion term.

The non-monotonic behavior observed in Fig. 13 is characteristic of large vortex strengths and can also be observed in the plots of the circulation. In Fig. 15 we display the time evolution of $\Gamma^+(t)$ for a fixed vortex strength $M_v = 1.7$ and a varying shock strength M_s from 2 to 7. For each plot, we marked with a $+$ the time t_3. We remark that the vorticity jump is strongly dependent on M_s but the shape of these plots remains roughly the same. For $M_s = 2$ and 2.5 the vortex is distorted by the shock wave, but only splits after some time; the positive circulation $\Gamma^+(t)$ is roughly monotonic in this case and it is only for $M_s \geqslant 3$, when separate vortical structures appear just after the interaction, that the $\Gamma^+(t)$ shows a distinctive non-monotonic behavior, together with a much more important net increase.

The non-monotonic behavior is not linked to the vortex breakdown, however. On Fig. 16, we explore the time evolution of $\Gamma^+(t)$ for a fixed strong shock, $M_s = 4$, and a varying vortex strength M_v from 0.5 to 1.7. The computational data confirms that larger vorticity jumps result from larger vortex strengths, but for $M_s = 4$ vortex breakdown occurs for all values of M_v considered in our parametric study, and in most cases, the behavior of $\Gamma^+(t)$ is roughly monotonic.

Therefore, from these observations it seems to be very difficult to give a relation between the production of circulation or vorticity and what we called the
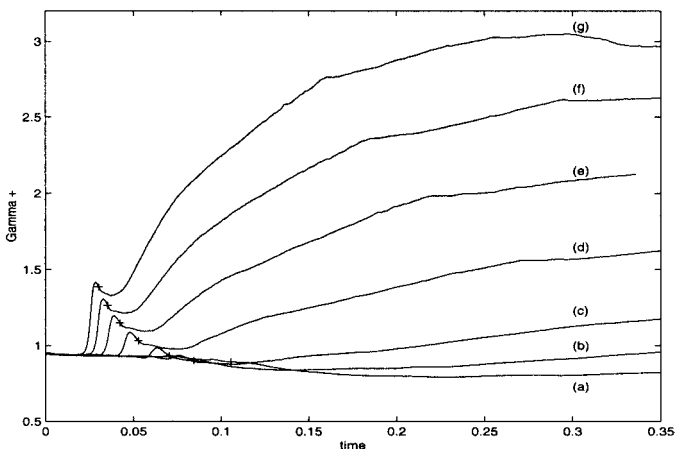

Fig. 15. Time evolution of $\Gamma^+(t)$ for $M_v = 1.7$ and $M_s = [2, 2.5, 3, 4, 5, 6, 7]$ from (a) $M_s = 2$ to (g) $M_s = 7$.
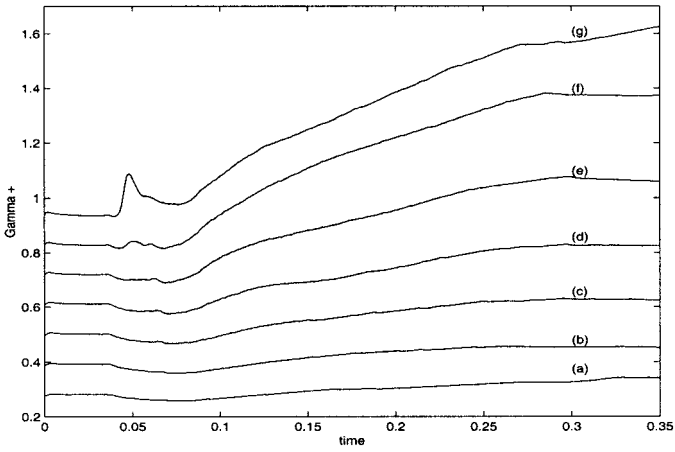
Fig. 16. Time evolution of $\Gamma^+(t)$ for $M_s = 4$ and $M_v = [0.5, 0.7, 0.9, 1.1, 1.3, 1.5, 1.7]$ from (a) $M_v = 0.5$ to (g) $M_v = 1.7$.

vortex breakdown. This could also be observed in Fig. 17 where we plot the maximum value of the enstrophy versus the parameters M_v and M_s. The maximum of enstrophy is an increasing function of these parameters, but it is rather small for weak vortices even in the case of large M_s, where the vortex is "broken" by the shock in at least two independent structures.

From our experiments we conjecture that the phenomenon we have denoted as vortex breakdown seems to be mainly due to the shock strength. A sufficiently
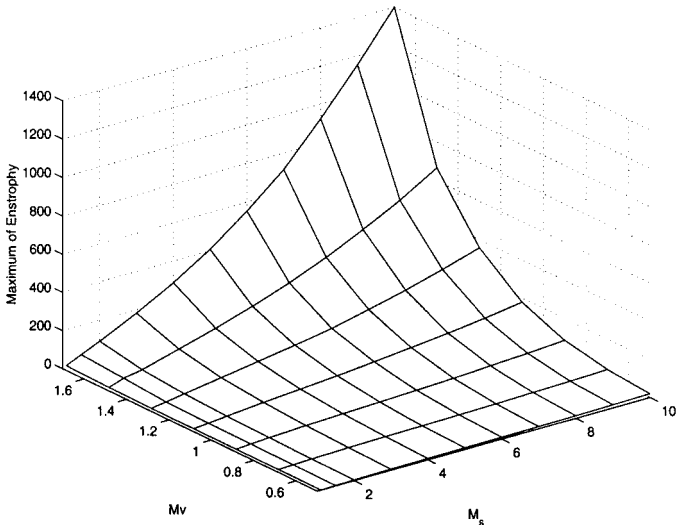

Fig. 17. Maximum of the enstrophy versus of the parameters M_v and M_s.

strong shock ($M_s > 3$ for this model) will so strongly disrupt the vorticity field that the outcome of the interaction will no longer be linked to one connected vortical structure. The initial vorticity influences more the number of structures that appear after the interaction (two or more).

6. COMPARISON WITH A THEORETICAL MODEL

Our empirical study demonstrates that the increase in enstrophy in the shock/vortex interaction is mainly driven by the expansion term. This should be compared with the conclusions in [22], where it is observed that the vorticity jump is dominated by the expansion term in turbulent regimes, in contrast to the results in [30] and [28] which show that the production of vorticity in the interaction of a shock with a density inhomogeneity, such as a bubble, is entirely baroclinic.

In [22], Kevlahan gives a general formula for the instantaneous jump in vorticity across a shock wave. He shows that the vorticity jump can be written as the sum of three terms, one directly related to the shock curvature and shock strength, one representing the baroclinic production and the third related to the conservation of angular momentum.

In this section we pay special attention to this last term—recall that in our case the baroclinic production has little influence—which, in the notation of [22], is

$$\delta\omega = \mu\omega_1, \qquad \mu = \frac{\rho_{bh}}{\rho_{ah}} - 1, \tag{9}$$

where ω_1 represents the vorticity ahead of the shock, μ is the normalized jump in density across the shock and ρ_{ah} and ρ_{bh} are the densities ahead and behind the shock.

Let us consider $\rho_{bh} = \rho_2$, the downstream density which depends on the shock strength, M_s. We fix M_v, the vortex strength and compute the vorticity jump given by (9) when ρ_{ah} is computed from (3) according to

- $\rho_{ah} = \rho_{r=0}$, the velocity at the center of the vortex (marked with the symbol "$*$" on Fig. 18),

- $\rho_{ah} = \rho_{r=a}$ (symbol "$+$"),

- $\rho_{ah} = \rho_{r=b} = \rho_1$ (symbol "$\times$").

We represent the values obtained for $1.1 \leqslant M_s \leqslant 10$, normalized by the corresponding value for $M_s = 1.1$, in Fig. 18. In addition, we compute

$$\delta\omega_{\text{num}} = \max_{x, y, t} |\omega_z| - \max_{x, y, t=0} |\omega_z|, \tag{10}$$

from our numerical data, normalize it by the corresponding value for $M_s = 1.1$ and display the result in Fig. 18 (symbol "O").

It is perhaps surprising to observe the good agreement between the normalized vorticity jump predicted by (9) when $\rho_{ah} = \rho_{r=a}$ and the computational one for $1.1 \leqslant M_s \lessapprox 6$ for $M_v = 1.7$ and $1.1 \leqslant M_s \lessapprox 7$ for $M_v = 1.5$. The agreement does not
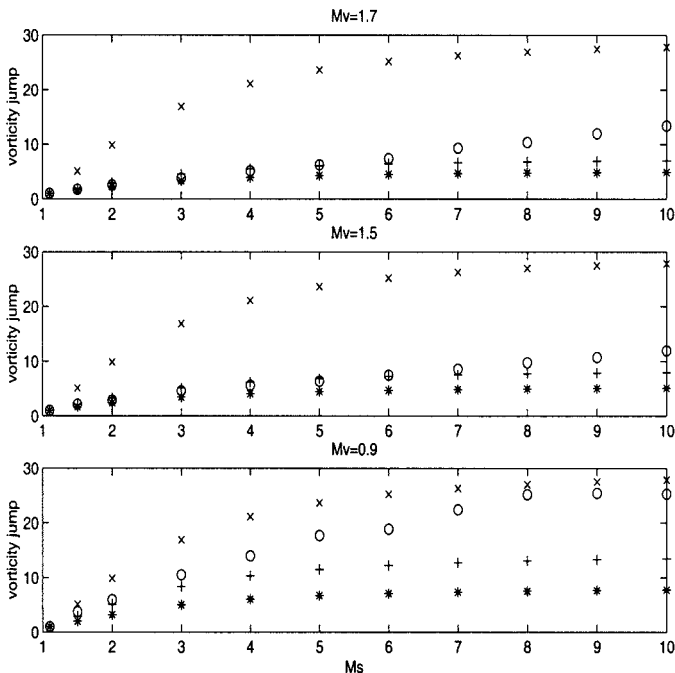
Fig. 18. Evolution of (normalized) $\mu\omega$ versus M_s for $M_v = 1.7$, $M_v = 1.5$ and $M_v = 0.9$. In each plot, "$*$" corresponds to $\rho_{ah} = \rho(r=0)$, "$+$" to $\rho_{ah} = \rho(r=a)$ and "$\times$" to $\rho_{ah} = \rho(r=b)$. The computed jump $\delta\omega_{num}$ is represented by "O." All quantities have been normalized by their value for $M_s = 1.1$.

hold for $M_v = 0.9$, but in all cases the computed values stay between the jump predicted by (9) for the values $\rho_{ah} = \rho_{r=0}$ and $\rho_{ah} = \rho_{r=b}$.

These results seem to indicate that for intense vortices (large M_v), where there is a large variation in the density field inside the vortex, the global increase in vorticity is mainly due to the vortex strength. On the contrary, when the rotation of the vortex is less intense and the density and pressure variations inside the vortex are much less important, a significant production of vorticity must be due to shock curvature.

These results are coherent with the remark of Kevlahan in [22] who states that $\mu\omega$ is the dominant term in the weak-shock turbulence interaction when *intense* vortices are present in the flow ahead of the shock.

7. CONCLUSIONS AND PERSPECTIVES

The difficulties in the numerical simulation of rotational flow inhomogeneities embedded in compressible flows has been recognized by many authors. In this paper we combine a particularly robust high resolution shock capturing scheme, the M-PHM scheme, with the multilevel work reduction technique developed in [4] to

obtain high resolution numerical simulations of a particular model of shock-vortex interaction. Our numerical technique, the M&M-PHM scheme, is able to obtain high quality, high resolution simulations of the complex shock structure that results at early times after the interaction as well as the late time evolution of the flow field, for a wide range of vortex and shock strengths. In particular we provide numerical simulations covering the strong-vortex/strong-shock case, which are rather scarce in the literature

We carry out a parametric study of the normal shock/vortex interaction and use the data in the numerical simulations to study the relative role of the different mechanisms responsible for the generation of vorticity in the interaction and its relation with the strong disruption of the vorticity field that occurs immediately after the encounter of a very strong shock with a vortex. We observe also that the disruption is more intense when increasing M_v, and that vorticity is generated in the interaction due, mainly, to expansion effects.

In addition, this work demonstrates the effectiveness of the M&M-PHM scheme for the numerical simulation of the shock-vortex interaction problem. We hope that our work will raise the level of awareness of the scientific community towards the potential of the M&M-PHM scheme in particular as an effective tool in analyzing not only qualitatively but also quantitatively, the structure and physical properties of complex flow fields.

ACKNOWLEDGMENTS

REFERENCES

1. Chatterjee, A. (1999). Shock wave deformation in shock-vortex interactions. *Shock Waves* **9**, 95–105.
2. Arandiga, F., Chiavassa, G., and Donat, R. (2001). *Application of Harten's Framework: From Conservation Laws to Image Compression*, Springer Lecture Notes in Computational Science and Engineering, Vol. 20, p. 281.
3. Cai, W., and Shu, C. W. (1993). Uniform high-order spectral methods for one and two dimensional Euler equations. *J. Comp. Phys.* **104**, 427–443.
4. Chiavassa, G., and Donat, R. (2001). Point value multiscale algorithm for 2D compressible flows. *SIAM J. Sci. Comp.* **23**(3), 805–823.
5. Chiavassa, G., Donat, R., and Marquina, A. (2001). Fine-mesh simulations for 2D Riemann problems with multilevel schemes. *International Series of Numerical Mathematics*, Vol. 140.
6. Chiavassa, G., Donat, R., and Marquina, A. (2000). A wavelet algorithm for 2D conservation laws. *Proceedings of Conference R. Temam, Equations aux derivées partielles non-linéaires: Applications à la mécanique des fluides et à la météorologie*, Poitiers.
7. Don, W. S. (1993). Numerical study of pseudospectral methods in shock waves applications. *J. Comp. Phys.* **104**.

8. Donat, R., Font, J. A., Ibànez, J. M., and Marquina, A. (1998). A flux-split algorithm applied to relativistic flows. *J. Comput. Phys.* **146**, 58–41.

9. Donat, R., and Marquina, A. (1996). Capturing shock reflections: An improved flux formula. *J. Comp. Phys.* **125**, 42.

10. Donat, R., and Marquina, A. (1999). Computing strong shocks in ultrarelativistic flows: A robust alternative. *International Series of Numerical Mathematics*, Vol. 129.

11. Dosanjh, D. S., and Weeks, T. M. (1965). Interaction of a starting vortex as well as a vortex street with a traveling shock wave. *AIAA J.* **3**, 216–223.

12. Einfeldt, B., Munz, C. D., Roe, P. L., and Sjörgreen, B. (1991). On godunov-type methods near low densities. *J. Comp. Phys..* **92**, 273–295.

13. Ellzey, J. L., Henneke, M. R., Picone, J. M., and Oran, E. S. (1995). The interaction of a shock with a vortex: Shock distortion and the production of acoustic waves. *Phys. Fluids* **7**, 172–184.

14. Erlebacher, G., Hussaini, M. Y., and Jackson, T. L. (1998). Nonlinear strong shock interactions: A shock fitted approach. *Theoret. Comput. Fluid Dynamics* **11**, 1–29.

15. Erlebacher, G., Hussaini, M. Y., and Shu, C. W. (1997). Interaction of a shock with a longitudinal vortex. *J. Fluid Mechanics* **337**, 129–153.

16. Fürst, J. (2001). *Modélisation numérique d'écoulements transsoniques avec des schémas TVD et ENO*, Ph.D. thesis, University of Aix-Marseille and of Praha.

17. Fürst, J., Angot, P., Debieve, J. F., and Kozel, K. (1997). Two and three-dimensional applications of TVD and ENO schemes, *Numerical Modelling in Continuum Mechanics, 3rd Summer Conf. in Praha, MATFIZPRESS Charles Univ.*, Vol. 1, pp. 103–111.

18. Fedkiw, R., Merriman, B., Donat, R., and Osher, S. (1997). The penultimate scheme for systems of conservation laws: Finite difference ENO with Marquina's flux splitting. In Hafez, M. M., and Chattot, J. J. (eds.), *Innovative Methods for Numerical Solutions of PDEs*, pp. 49–85.

19. Grasso, F., and Pirozzoli, S. (2000). Shock-wave–vortex interactions: Shock and vortex deformations and sound production. *Theoret. Comput. Fluid Dynamics* **13**, 421–456.

20. Inoue, O., and Hattori, Y. (1999). Sound generation by shock-vortex interactions. *J. Fluid Mech.* **380**, 81–116.

21. Jiang, G. S., and Shu, C. W. (1996). Efficient implementation of weighted ENO schemes. *J. Comput. Phys.* **126**, 202–228.

22. Kevlahan, N. K.-R. (1997). The vorticity jump across a shock in a non-uniform flow. *J. Fluid Mech.* **341**, 371–384.

23. Marquina, A., and Mulet, P. A flux-split algorithm applied to conservative models for multicomponent compressible flows. To appear in *J. Comput. Phys.*

24. Marquina, A. (1994). Local piecewise hyperbolic reconstruction of numerical fluxes for nonlinear scalar conservation laws. *SIAM J. Sci. Comput.* **15**, 892–915.

25. Meadows, K. R., Kumar, A., and Hussaini, M. Y. (1991). Computational study on the interaction between a vortex and a shock wave, *AIAA J.* **29**(2), 174–179.

26. Naumann, A., and Hermanns, E. (1973). On the interaction between a shock wave and a vortex field. *AGARD CP* 131.

27. Pao, S. P., and Salas, M. D. (1981). *A Numerical Study of Two-Dimensional Shock-Vortex Interaction*, AIAA paper AIAA-81-1205. 14th Fluid and Plasma Dynamics Conference.

28. Picone, J. M., and Boris, J. P. (1988). Vorticity generation by shock propagation through bubbles in a gas. *J. Fluid Mech.* **189**, 23–51.

29. Ribner, H. S. (1985). Cylindrical sound waves generated by shock-vortex interaction. *AIAA J.* **23**(11), 1708–1715.

30. Samtaney, R., and Zabusky, N. J. (1994). Circulation deposition on shock-accelerated planar and curved density-stratified interfaces: Models and scaling laws. *J. Fluid Mech.* **269**, 45–78.

31. Shu, C. W., and Osher, S. J. (1989). Efficient implementation of essentially non-oscillatory shock-capturing schemes II. *J. Comp. Phys.* **83**, 32–78.

32. Smart, M. K., Kalkhoran, I. M., and Popovic, S. (1998). Some aspects of streamwise vortex behavior during oblique shock wave/vortex interaction. *Shock Waves* **8**, 243–255.

33. Toro, E. F. (1999). *Riemann Solvers and Numerical Methods for Fluid Dynamics*, Springer-Verlag.